surrounding Earth and the proto-lunar disc as the Moon solidified (*32*). Alternatively, it is conceivable that a portion of the lunar interior escaped the widespread melting and degassing expected in the aftermath of a giant impact and simply inherited water from the proto-Earth. The latter alternative is consistent with the hypothesis that the Moon began with a 200- to 300-km-thick outer shell near melting conditions and a relatively cold interior (*33*). This hypothesis has received support from recent gravity gradiometry observations by the Gravity Recovery and Interior Laboratory (GRAIL) (*34*). Any dynamic model proposed for the formation of the Earth-Moon system must meet the constraints imposed by the presence of H_2O with an isotopic composition similar to that of terrestrial water in the lunar interior.

Our findings also have implications for the origin of water ice in permanently shadowed lunar craters, which has been attributed to solar wind implantation and to cometary and meteoritic impacts (*21*). It is conceivable that at least part of this water could have originated from magmatic degassing during lunar volcanic eruptions.

References and Notes

1. A. Morbidelli *et al.*, *Meteorit. Planet. Sci.* **35**, 1309 (2000).
2. K. J. Walsh, A. Morbidelli, S. N. Raymond, D. P. O'Brien, A. M. Mandell, *Meteorit. Planet. Sci.* **47**, 1941 (2012).
3. C. M. Alexander *et al.*, *Science* **337**, 721 (2012).
4. A. N. Halliday, *Geochim. Cosmochim. Acta* **105**, 146 (2013).
5. B. Marty, *Earth Planet. Sci. Lett.* **313-314**, 56 (2012).
6. F. Robert, *Science* **293**, 1056 (2001).
7. F. Robert, Solar System Deuterium/Hydrogen ratio, in *Meteorites and the Early Solar System II*, D. S. Lauretta, H. Y. McSween Jr., Eds. (Univ. of Arizona Press, Tucson, AZ, 2006), pp. 341–352.
8. D/H is also expressed as $\delta D = \{[(D/H)_{sample}/(D/H)_{VSMOW}] - 1\} \times 1000$; VSMOW: Vienna standard mean ocean water.
9. C. Lécuyer, P. Gillet, F. Robert, *Chem. Geol.* **145**, 249 (1998).
10. P. Hartogh *et al.*, *Nature* **478**, 218 (2011).
11. K. Lodders, R. Osborne, *Space Sci. Rev.* **90**, 289 (1999).
12. R. M. Canup, *Science* **338**, 1052 (2012).
13. M. Ćuk, S. T. Stewart, *Science* **338**, 1047 (2012).
14. C. K. Shearer *et al.*, *Rev. Mineral. Geochem.* **60**, 365 (2006).
15. A. E. Saal *et al.*, *Nature* **454**, 192 (2008).
16. J. W. Boyce *et al.*, *Nature* **466**, 466 (2010).
17. F. M. McCubbin *et al.*, *Proc. Natl. Acad. Sci. U.S.A.* **107**, 11223 (2010).
18. J. P. Greenwood *et al.*, *Nat. Geosci.* **4**, 79 (2011).
19. E. H. Hauri, T. Weinreich, A. E. Saal, M. C. Rutherford, J. A. Van Orman, *Science* **333**, 213 (2011).
20. H. Hui, A. H. Peslier, Y. Zhang, C. R. Neal, *Nat. Geosci.* **6**, 177 (2013).
21. Supplementary materials are available on *Science* Online.
22. L. Merlivat, M. Lelu, G. Neif, E. Roth, *Proc. Lunar Planet. Sci. Conf.* **7**, 649 (1976).
23. R. C. Reedy, *Proc. Lunar Planet. Sci. Conf.* **12**, 871 (1981).
24. R. R. Spangler, R. Warasila, J. W. Delano, *Proc. Lunar Planet. Sci. Conf.* **14**, 487 (1984).
25. O. Eugster, N. Groegler, P. Eberhardt, J. Geiss, W. Kiesl, *Proc. Lunar Planet. Sci. Conf.* **12**, 541 (1981).
26. Y. Zhang, H. Ni, *Rev. Mineral. Geochem.* **72**, 171 (2010).
27. M. M. Hirschmann, A. C. Withers, P. Ardia, N. T. Foley, *Earth Planet. Sci. Lett.* **345-348**, 38 (2012).
28. E. H. Hauri, *Chem. Geol.* **183**, 115 (2002).
29. C. M. Weitz, M. J. Rutherford, J. W. Head III, D. S. McKay, *Meteorit. Planet. Sci.* **34**, 527 (1999).
30. B. Marty, K. Hashizume, M. Chaussidon, R. Wieler, *Space Sci. Rev.* **106**, 175 (2003).
31. J. M. D. Day, D. G. Pearson, L. A. Taylor, *Science* **315**, 217 (2007).
32. K. Pahlevan, D. J. Stevenson, J. M. Eiler, *Earth Planet. Sci. Lett.* **301**, 433 (2011).
33. S. C. Solomon, J. Chaiken, *Proc. Lunar Planet. Sci. Conf.* **7**, 541 (1976).
34. J. C. Andrews-Hanna *et al.*, *Science* **339**, 675 (2013).

Acknowledgments: We are grateful to A. Halliday, P. Warren, D. Stevenson, A. Morbidelli, K. Walsh, C. Alexander, A. Davis, and B. Marty for discussion, and thank the anonymous reviewers for discussion, criticism, and advice. We thank J. Wang for expert assistance with the NanoSIMS. This work was funded by NASA Cosmochemistry NNX12AH62G and LASER NNX08AY97G programs, and by the Brown–Massachusetts Institute of Technology NASA Lunar Science Institute NNA09DB34A.

Supplementary Materials

www.sciencemag.org/cgi/content/full/science.1235142/DC1
Materials and Methods
Supplementary Text
Figs. S1 and S2
Table S1
References (*35*–*103*)

14 January 2013; accepted 25 April 2013
Published online 9 May 2013;
10.1126/science.1235142

Clarifying the Dominant Sources and Mechanisms of Cirrus Cloud Formation

Daniel J. Cziczo,[1]* Karl D. Froyd,[2,3] Corinna Hoose,[4] Eric J. Jensen,[5] Minghui Diao,[6] Mark A. Zondlo,[6] Jessica B. Smith,[7] Cynthia H. Twohy,[8] Daniel M. Murphy[2]

Formation of cirrus clouds depends on the availability of ice nuclei to begin condensation of atmospheric water vapor. Although it is known that only a small fraction of atmospheric aerosols are efficient ice nuclei, the critical ingredients that make those aerosols so effective have not been established. We have determined in situ the composition of the residual particles within cirrus crystals after the ice was sublimated. Our results demonstrate that mineral dust and metallic particles are the dominant source of residual particles, whereas sulfate and organic particles are underrepresented, and elemental carbon and biological materials are essentially absent. Further, composition analysis combined with relative humidity measurements suggests that heterogeneous freezing was the dominant formation mechanism of these clouds.

The effect of clouds on the climate system is more uncertain than the influence of heat-trapping greenhouse gases (*1*). Clouds can cool by reflection of solar radiation and warm by trapping terrestrial heat with the balance of effects depending on cloud properties such as altitude, thickness, phase, and droplet or crystal size (*2*). Cirrus clouds are of particular importance because they have extensive global coverage and occur high in the atmosphere, at altitudes of 8 to 17 km (*2*). Global modeling suggests that human effects on ice clouds may rival the radiative effect of all anthropogenic aerosol particles that do not participate in cloud formation (*3*).

Due to the temperature at their altitude of formation, cirrus clouds are composed exclusively of ice crystals (*2*). Ice nucleation does not take place directly from water vapor but instead requires a preexisting particle (*4*). Ice forms via two pathways, termed homogeneous and heterogeneous freezing. Homogeneous freezing, the spontaneous nucleation of ice within a sufficiently cooled solution, is better understood. A simple theoretical framework for this process has been developed for use in model studies (*5*). Because the vast majority of atmospheric aerosol particles are aqueous solutions of sulfates and organic molecules (*6*), homogeneous freezing has been assumed the dominant process (*7*). However, one drawback to homogeneous freezing is that relative humidity must be strongly supersaturated with respect to ice (RH_i = 150 to 170%) (*4*, *8*). In contrast, heterogeneous freezing can start just below 0°C and at $RH_i \sim 100\%$ (*2*, *8*). Heterogeneous freezing remains poorly understood, however, because it can take several subpathways, among which are depositional freezing of water vapor onto a particle surface and immersion freezing from within an aqueous coating (*4*). Many materials have been shown to act as ice nuclei (IN) in laboratory experiments, including mineral dust, metallic particles, some biological materials, low-temperature glasses, and anhydrous salts (*4*, *9*–*11*). Despite this variety, only a small fraction of atmospheric particles at ground level (as few as ~1 in 10^5) have been shown to act as IN (*4*, *8*).

[1]Department of Earth, Atmospheric and Planetary Sciences, Massachusetts Institute of Technology, 77 Massachusetts Avenue, Cambridge, MA 02139, USA. [2]National Oceanic and Atmospheric Administration Earth System Research Laboratory, Chemical Sciences Division, Boulder, CO 80305, USA. [3]Cooperative Institute for Research in Environmental Science, University of Colorado, Boulder, CO 80309, USA. [4]Institute for Meteorology and Climate Research–Atmospheric Aerosol Research, Karlsruhe Institute of Technology, 76021 Karlsruhe, Germany. [5]NASA Ames Research Center, Moffett Field, CA 94035, USA. [6]Department of Civil and Environmental Engineering, Princeton University, Princeton, NJ 08544, USA. [7]School of Engineering and Applied Sciences, Harvard University, Cambridge, MA 02138, USA. [8]College of Earth, Ocean, and Atmospheric Sciences, Oregon State University, Corvallis, OR 97331, USA.

*Corresponding author. E-mail: djcziczo@mit.edu

Here, we have determined the chemical and physical properties of the particles on which cirrus ice crystals formed from measurements acquired aboard two NASA research aircraft. These data reveal the particle types that are relevant for cirrus formation, from which we can infer the ice nucleation mechanism. We term the material within an ice crystal an ice residual (IR) because particles and gases may be scavenged after ice nucleation. Our data do not indicate multiple particles per IR, and the low pressure and number density of particles in the cirrus regime render it unlikely that scavenging represents a distinct artifact (*12*).

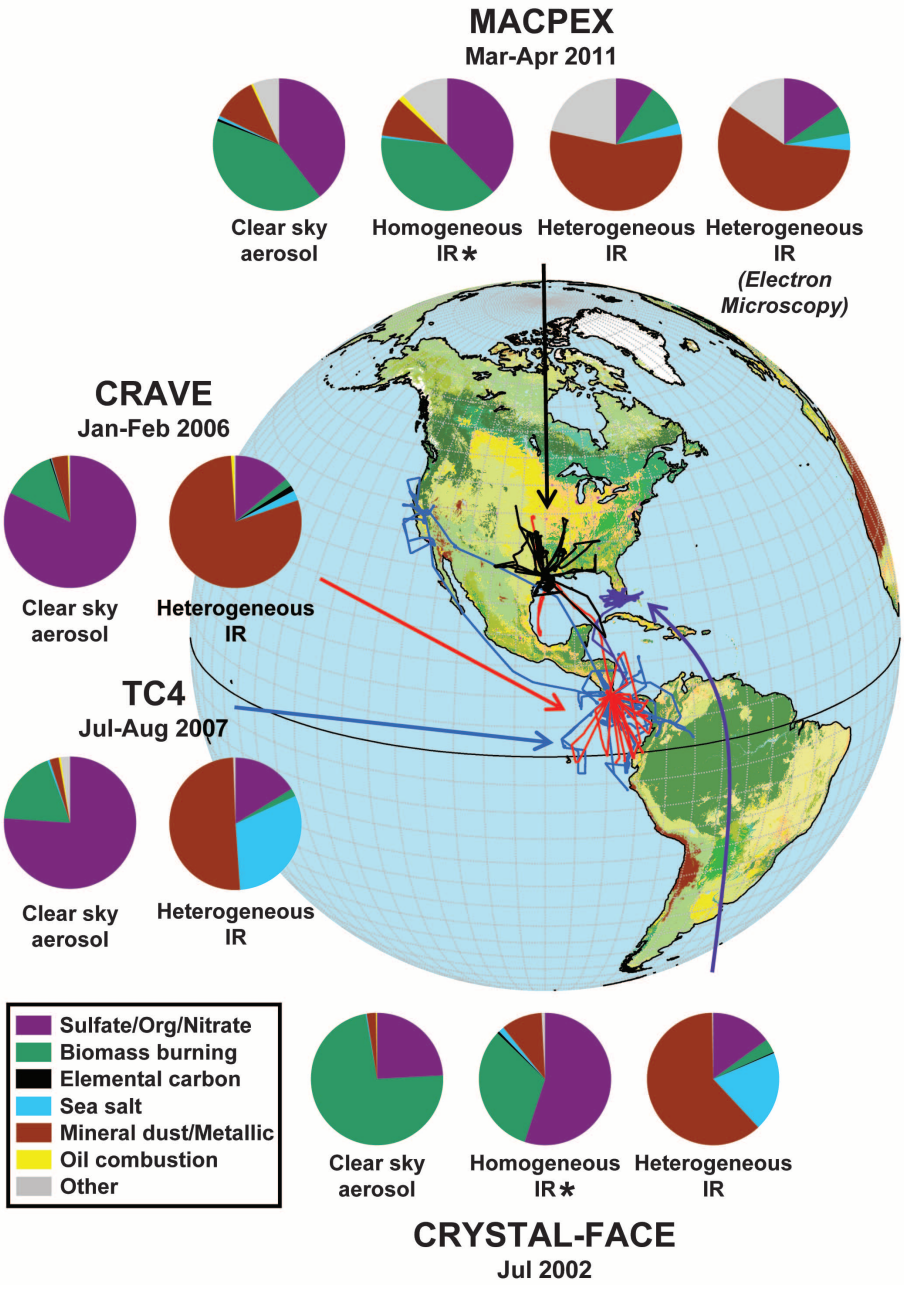

Fig. 1. Flight tracks of ice cloud–residual measurements for four aircraft campaigns spanning a range of geographic regions and seasons. The composition of cirrus IRs and near-cloud aerosol, on a number basis, are summarized for each campaign. Ice-crystal separation was accomplished with a counterflow virtual impactor inlet, and composition was determined by single-particle mass spectrometry (MS) where individual particles were desorbed and ionized with a 193-nm wavelength excimer laser and ion abundance was measured with time-of-flight MS (*13*, *14*). This technique is sensitive to all atmospheric aerosol particle components in a range from ~0.2- to 3-μm aerodynamic diameter (*13*, *14*). IR particles were also collected and analyzed with EM coupled to energy-dispersive x-ray microanalysis (*21*). Homogeneous freezing appeared to initiate cloud formation for only two individual cirrus clouds with composition shown in two insets (denoted by asterisks). Mineral dust is the most dominant heterogeneous ice nucleus in all other cirrus encounters despite the geographic separation between the study areas and major global dust sources, shown in brown (NASA Land Processes Distributed Active Archive Center, https://lpdaac.usgs.gov/get_data).

Between 2002 and 2011, we conducted four aircraft measurement campaigns, designed to sample within regions of high cirrus cloud abundance, over North and Central America and nearby ocean (Fig. 1). Data from liquid water–containing clouds are excluded. Tropical tropopause cirrus clouds were previously considered (*13*). These clouds, which can have extensive coverage in the tropics, have been shown to consist of a low number density of relatively small ice crystals that probably formed heterogeneously on glassy aerosols or anhydrous salts (*13*). Measurements were taken in air-traffic corridors, although contrails were not specifically targeted. We then combined mass spectra for thousands of individual IRs and near-cloud aerosol (Fig. 2) into seven categories (Fig. 1). The mode of freezing is inferred from the relative composition: When the IRs were predominantly sulfate and/or organic and similar to the near-cloud particles, homogeneous freezing is inferred, whereas dissimilar IRs and near-cloud particles indicate heterogeneous nucleation (*8*, *14*). Based on these criteria, the freezing mechanism was heterogeneous in 94% of cloud encounters.

The predominant particle category on which freezing took place was mineral dust and metallic particles, at 61% (Fig. 1). This category was also the most enhanced in cloud ice, with respect to its near-cloud abundance (5%). The overwhelming majority (~90%) of particles exhibit no apparent sulfate or organic coating. Mixtures of sulfate and organic carbon—in all cases, the largest near-cloud category at 55%—were the principal IRs in only two distinct cloud encounters for which homogeneous freezing is inferred. In all other cirrus clouds, sulfate and organic particles were 14% of the IRs. Sulfate and organic material can act as IN when present as glasses or anhydrous salts (*10*, *11*). Therefore, some of these particles may have entered the ice phase heterogeneously, implying that the 94% value of heterogeneous freezing may be a lower limit. Sea salt was abundant as IR (at 25%) during flights that took place over open ocean but was only 3% IR during other flights. In all cases, biomass burning was the second most near-cloud–abundant particle type (36%) but was depleted in the IR, representing <5%. These quantities represent composite averages for each of the four campaigns. We individually analyzed single flights within campaigns, with the only differences from the campaign averages being the homogeneous freezing cases (*12*). Representative spectra are shown for four IR types in Fig. 2.

The cirrus encounters presented here include both convective outflow and synoptically formed clouds. Because of the updrafts in convection, the aerosols immediately next to these clouds may not be representative of those within. Analyzed separately, we find that mineral dust and metallic

particles are the dominant IRs, regardless of cirrus type, when heterogeneous freezing was inferred (56% in clouds associated with convection and 63% in those without). We therefore believe this result is consistent across cirrus-development scenarios. Individual field study values are provided in Fig. 1 (*12*).

Relative humidity measurements can also be used to constrain cirrus-formation mechanisms (*15*, *16*). Clear-sky (cloud-free) RH_i measurements taken during the flights on which IR data were collected are shown as a function of temperature in Fig. 3, along with measurements from three campaigns spanning a larger geographic area (*17*, *18*). Sampling locations include North and Central America, the western Atlantic, and an area spanning from the central Pacific to the Arctic. At cirrus temperatures, <3% of the clear-sky RH_i data exceed ~140%, a humidity consistent with heterogeneous freezing of mineral dust (*2*, *4*). Less than 0.5% of the RH_i data surpass the

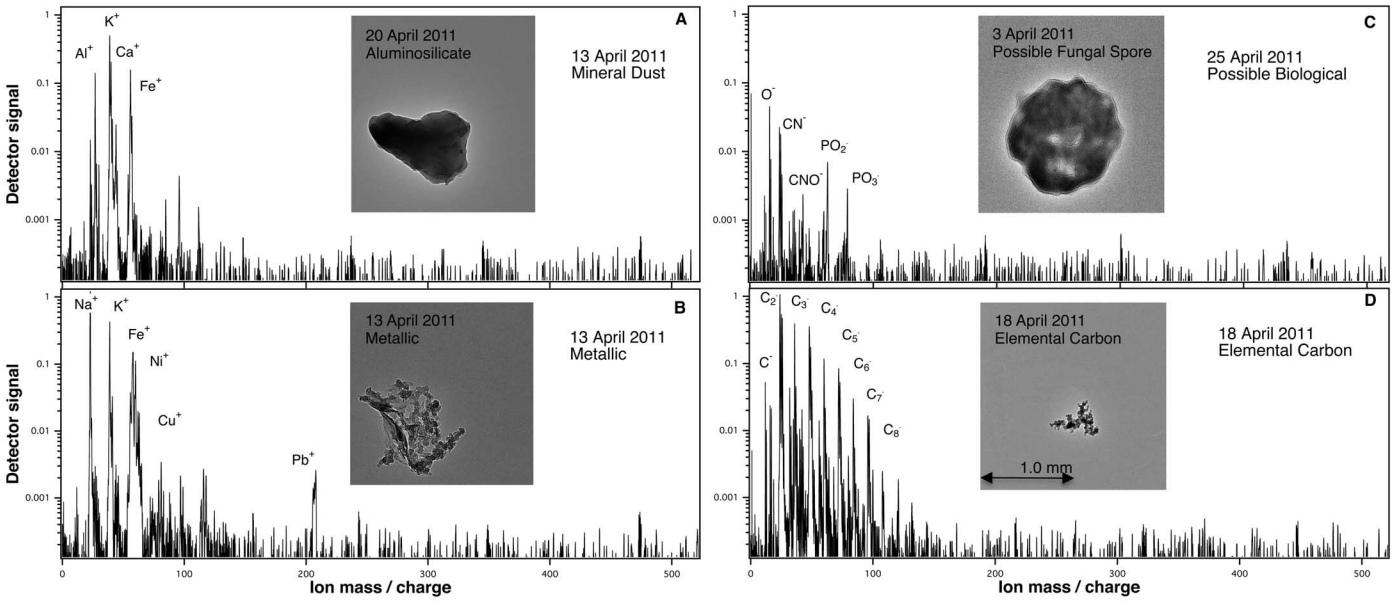

Fig. 2. Single-particle MS and EM (inset) images of IR particles, analyzed during the MACPEX aircraft campaign, corresponding to the categories presented in Fig. 1. (**A**) MS: the most common residual mineral dust with minimal surface coating; EM: an aluminosilicate particle, also without apparent surface coating. (**B**) MS: metallic particle with sodium, potassium, nickel, copper, iron, and lead; EM: metallic particle with tin, carbon, and silicon. (**C**) MS: one of six particles of possible biological origin suggested by a composition including carbon, nitrogen, oxygen, and phosphorous (*12*); EM: the only particle of possible biological origin found on the electron microscope grids suggested by a composition including carbon, hydrogen, oxygen, and phosphorous. (**D**) MS: an EC particle; EM: one of two EC particles, identified by both composition and fractal spherule aggregate structure. Note that the spectra and images do not correspond to the same particles.

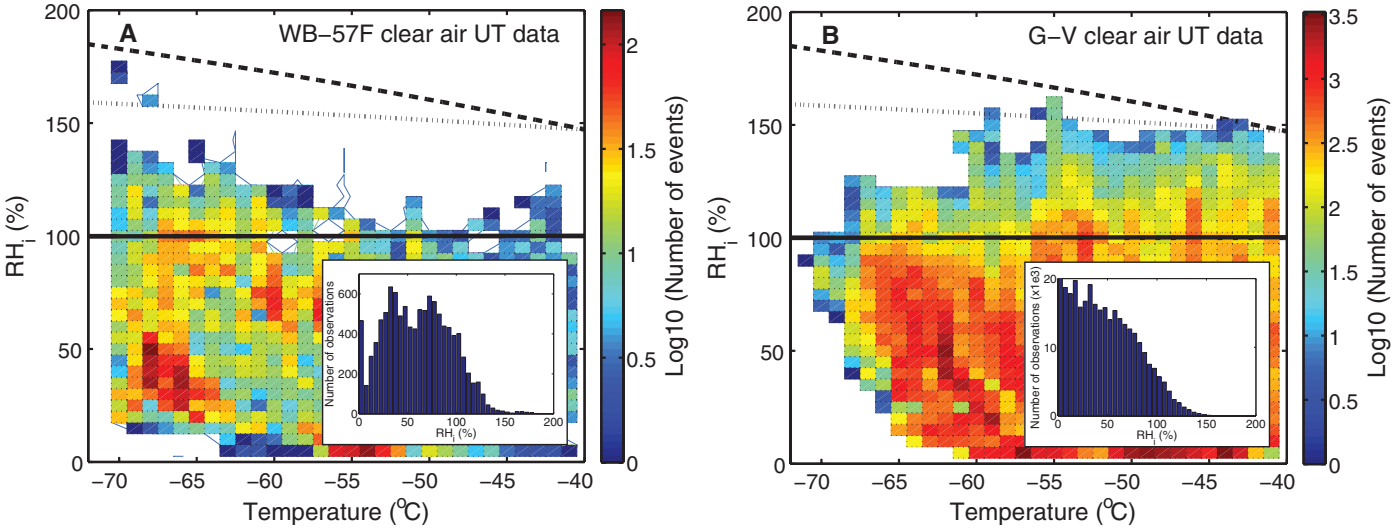

Fig. 3. Distribution of upper tropospheric, clear-air relative humidity with respect to ice (RH_i) as a function of temperature. Color-coding corresponds to the number of events observed in each 5% RH_i and 1°C bin. The dashed and solid lines indicate ice and liquid water saturation, respectively. (**A**) Composite of data collected in conjunction with the IR data shown in Figs. 1 and 2. The inset depicts a histogram of these data for temperatures warmer than –70°C. Greater than 99% of the RH_i data in this temperature range fall below the threshold for homogeneous nucleation, denoted by the dotted lines. (**B**) Composite of data collected over a larger geographical area onboard the NSF G-V aircraft. The RH_i data account for water vapor mixing ratios measured by the Harvard Water Vapor instrument (*17*) and the Vertical Cavity Surface Emitting Laser hygrometer (*18*). Inset to (B), same as in (A). UT, universal time.

threshold for homogeneous freezing, also suggesting that heterogeneous freezing is the dominant formation mechanism.

Because ice-crystal number densities ranging from 1s to 100s per liter are consistent with heterogeneous freezing, whereas larger abundances are indicative of homogeneous nucleation (*19*), these measurements offer a third constraint on ice-formation mechanisms. Recently realized artifacts associated with ice-crystal shattering and consequent overcounting of number density render many previous conclusions uncertain. Higher-confidence data from the most recent set of flights indicate that only a few percent of clouds have number densities greater than a few hundred per liter (*19*). The combination of in situ determination of IR composition, relative humidity measurements, and ice-crystal number densities from multiple field campaigns in different regions presents a compelling case to consider heterogeneous freezing the dominant mechanism of cirrus formation throughout the study regions. These data stand in contrast to recent model studies that suggest the opposite conclusion (*7*).

Mineral dust is ubiquitous in the atmosphere (*20*). In agreement with the data presented here, collections of snow and cloud samples have shown mineral dust to be the predominant atmospheric IN (*4*, *8*, *14*, *21*, *22*). Ground-based and laboratory studies that nucleate ice under controlled conditions also show mineral dust to be effective as IN at <–10°C and RH_i from 110 to 140% (*3*). Laboratory studies show that sulfate and organic surface coatings "deactivate" mineral dust particles, rendering them less effective as IN (*23*), consistent with our results. Analysis of mineral dust particles collected in the free troposphere shows that uncoated particles are present thousands of kilometers from their source (*24*). Our data show that the uncoated subset of mineral dust—likely composed of particles that have not undergone substantial aging or a cloud-processing event—is the most important. The climatological importance of mineral dust is consistently demonstrated by laboratory studies that characterize it as an effective ice nucleus, field studies that observe its presence in the free troposphere, and IR analyses that show it dominates within ice crystals. In regions where the concentration of mineral dust and metallic aerosol is low, such as the high latitudes of the Southern Hemisphere, homogeneous freezing or ice nucleation by glassy particles and anhydrous salts (*10*, *11*) may be of greater importance than observed in these studies.

The lack of elemental carbon (EC) and biological particles is notable. Neither was abundant in the near-cloud particles or the ice phase, representing <1% in all cases. The in situ results are supported by IR collection for offline electron microscopy (EM) compositional analysis (*12*, *21*, *22*) during the most recent set of flights. We observed only a single possible biological particle and two EC IR particles during these flights, representing <<1%.

With few exceptions, laboratory studies of EC have shown these particles to be inefficient IN, with nucleation only at temperatures and supersaturations close to homogeneous freezing (*9*, *25*). We conclude that effective ice-nucleating EC particles are of low abundance in the cirrus regime. However, this finding may not be valid in contrails, which were not studied. Our 2002 and 2011 measurements are noteworthy: wildfires injected EC- and biomass-burning particles into the upper tropospheric study region, yet these particles were not abundant as IRs. Thus, we suggest models ignore EC as an ice-forming particle type for cirrus clouds.

The case of biological particles is more complex than those of mineral dust and EC. Laboratory studies have shown that a few types of bacteria and fungal spores act as effective IN (*9*, *26*). Field results, which include collections of ice-phase precipitation and residues from one orographic cloud, sometimes show the presence of biological material (*27*). Particle-phase scavenging is a greater concern in precipitation studies than in those of cirrus clouds, but nonetheless, these results suggest that a subset of biological particles are effective IN. The upper tropospheric data set reported here does not support an abundance of biological material as IRs, widespread internal mixing with mineral dust, or the simple identification suggested in other studies (*12*, *27*). This data set suggests that most biological particles generated at Earth's surface are removed via dry or wet deposition due to their large size and water- or ice-nucleating potential before they are transported to cirrus altitude. We recommend that models ignore biological material as a cirrus-forming particle type. The discrepancy between this and lower altitude studies suggests a fundamental difference between measurements made within or coupled to the boundary layer and those made in the mid- to upper troposphere. Furthermore, the lower-altitude IR data were obtained in a cloud with ice crystals considerably larger than those we have been able to sample without impaction artifacts (*12*), although even in that study, mineral dust residuals dominated over biological particles (*27*).

Metallic particles represent an IR particle type that has not been extensively studied in the laboratory. Our data include a diversity of species such as Pb, Zn, Sn, Cu, Ag, Mo, and other heavy metals that have low abundance in mineral dust (Fig. 2). These metals were present in elemental, oxide, and sulfate forms. During the most recent set of flights, metallic particles represented 9 to 26% of the IRs. A few previous field studies have noted metal-rich "industrial" IN (*4*, *8*, *28*, *29*). Lead, present in ~5% of ambient particles (*30*), has been shown to be a particularly efficient ice nucleus in the field and the laboratory (*21*, *29*). Laboratory studies and improved emission inventories coupled to cloud-formation models are needed to elucidate the global effect of anthropogenic particles on cirrus clouds.

Both the number and activity of heterogeneous IN control the formation of cirrus clouds. A global simulation of upper tropospheric aerosol-particle concentrations combined with laboratory measurements of IN were used to predict cirrus formation. Independent of the IR composition measurements, this analysis also asserts the dominance of mineral dust among cirrus IN (*9*, *12*, *31*, *32*) (Fig. 4). In both depositional- and immersion-freezing modes, mineral dust contributes the largest number of free tropospheric IN. Laboratory studies of EC suggest a wide range of IN efficiencies. In only the extreme case where all EC is assumed to have the highest efficiency does this species rival mineral dust. Biological particles are shown to be extremely rare in the upper troposphere, rendering them unable to compete with mineral dust in the cirrus temperature range (<–30°C). Although many air parcels originating from mineral-dust emission areas undergo cloud processing before reaching cirrus altitudes (*20*), resulting in depletion and/or coating of these particles, no comprehensive global data measurements of the aerosol coating state exist and, thus, are not included in this model. The scarcity of laboratory experiments on biomass burning and metallic particles render us unable to provide separate estimates for these species.

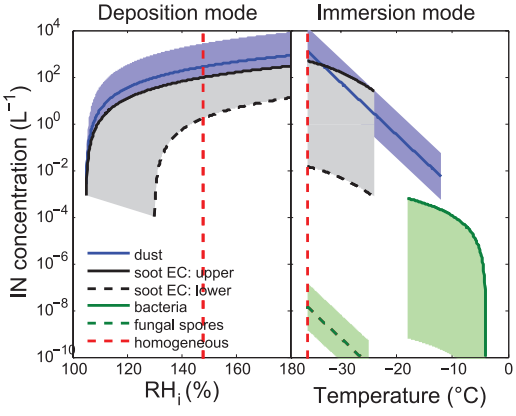

Fig. 4. Estimates of upper tropospheric IN concentration versus RH_i and temperature from global simulations of aerosol surface area concentration and ice nucleation active site (INAS) densities derived from various laboratory experiments (*12*). Estimates of upper tropospheric IN concentrations and annual average aerosol particle concentration from two versions of the CAM-Oslo model (*31*, *32*) were used. These estimates are derived independently from the in situ data. Deposition (between −35° and −57°C) and immersion nucleation modes are considered separately. The onset of homogeneous freezing is indicated by the red dashed lines for an approximate freezing rate coefficient of 5×10^{14} m^{-3} s^{-1}. Shaded areas represent the range of measured INAS densities.

References and Notes

1. S. Solomon, Ed., *Climate Change 2007: The Physical Science Basis. Contribution of Working Group I to the Fourth Assessment Report of the Intergovernmental Panel on Climate Change* (Cambridge Univ. Press, Cambridge, 2007).
2. D. K. Lynch, K. Sassen, D. C. Starr, G. Stephens, Eds., *Cirrus* (Oxford Univ. Press, New York, 2002).
3. U. Lohmann, *Geophys. Res. Lett.* **29**, 11-1 (2002).
4. H. R. Pruppacher, J. D. Klett, in *Microphysics of Clouds and Precipitation* (Kluwer Academic, Dordrecht, ed. 2, 1997), pp. 309–354.
5. T. Koop, B. P. Luo, A. Tsias, T. Peter, *Nature* **406**, 611 (2000).
6. D. M. Murphy, D. S. Thomson, M. J. Mahoney, *Science* **282**, 1664 (1998).
7. A. Gettelman, X. Liu, D. Barahona, U. Lohmann, C. Chen, *J. Geophys. Res.* **117**, D20201 (2012).
8. P. J. DeMott *et al.*, *Proc. Natl. Acad. Sci. U.S.A.* **100**, 14655 (2003).
9. C. Hoose, O. Möhler, *Atmos. Chem. Phys.* **12**, 9817 (2012).
10. B. J. Murray *et al.*, *Nat. Geosci.* **3**, 233 (2010).
11. J. P. D. Abbatt *et al.*, *Science* **313**, 1770 (2006).
12. Materials and methods are available as supplementary materials on *Science* Online.
13. K. D. Froyd, D. M. Murphy, P. Lawson, D. Baumgardner, R. Herman, *Atmos. Chem. Phys.* **10**, 209 (2010).
14. D. J. Cziczo, D. M. Murphy, P. K. Hudson, D. S. Thomson, *J. Geophys. Res.* **109**, D04201 (2004).
15. A. J. Heymsfield, L. M. Miloshevich, C. Twohy, G. Sachse, S. Oltmans, *Geophys. Res. Lett.* **25**, 1343 (1998).
16. M. Krämer *et al.*, *Atmos. Chem. Phys.* **9**, 3505 (2009).
17. E. M. Weinstock *et al.*, *Rev. Sci. Instrum.* **65**, 3544 (1994).
18. M. A. Zondlo, M. E. Paige, S. M. Massick, J. A. Silver, *J. Geophys. Res.* **115**, D20309 (2010).
19. E. J. Jensen, P. Leonhard, P. Lawson, paper presented at the 16th International Conference on Clouds and Precipitation, Leipzig, Germany, 31 July 2012.
20. A. Wiacek, T. Peter, U. Lohmann, *Atmos. Chem. Phys.* **10**, 8649 (2010).
21. M. Ebert *et al.*, *Atmos. Chem. Phys.* **11**, 2805 (2011).
22. A. C. Targino, R. Krejci, K. J. Noone, P. Glantz, *Atmos. Chem. Phys.* **6**, 1977 (2006).
23. D. J. Cziczo *et al.*, *Environ. Res. Lett.* **4**, 044013 (2009).
24. T. Kojima, P. R. Buseck, Y. Iwasaka, A. Matsuki, D. Trochkine, *Atmos. Res.* **82**, 698 (2006).
25. M. Dymarska *et al.*, *J. Geophys. Res.* **111**, D04204 (2006).
26. O. Möhler, P. J. DeMott, G. Vali, Z. Levin, *Biogeosciences* **4**, 1059 (2007).
27. K. A. Pratt *et al.*, *Nat. Geosci.* **2**, 398 (2009).
28. C. H. Twohy, M. R. Poellot, *Atmos. Chem. Phys.* **5**, 2289 (2005).
29. D. J. Cziczo *et al.*, *Nat. Geosci.* **2**, 333 (2009).
30. D. M. Murphy *et al.*, *Atmos. Chem. Phys.* **7**, 3195 (2007).
31. A. Kirkevåg *et al.*, *Geosci. Model Dev.* **6**, 207 (2013).
32. C. Hoose, J. E. Kristjánsson, S. M. Burrows, *Environ. Res. Lett.* **5**, 024009 (2010).

Acknowledgments: We thank D. S. Thomson and G. Kulkarni for assistance with the measurements; S. Solomon for advice on manuscript preparation; all participants of the field studies for their efforts, in particular the air and ground crews of the NASA WB-57F and DC-8 and NSF G-V; and O. Seland, D. Olivié, and A. Kirkevåg for providing particle surface area densities from CAM4-Oslo simulations. The MDC12C1 2011 Land Cover Type data were obtained through the online Data Pool at the NASA Land Processes Distributed Active Archive Center, U.S. Geological Survey/Earth Resources Observation and Science Center, Sioux Falls, South Dakota (https://lpdaac.usgs.gov/get_data). M.A.Z. acknowledges support from NSF AGS-0840732 and AGS-1036275, M.D. acknowledges a NASA Earth and Space Science Graduate Fellowship, and C.H.T. acknowledges support from the NASA Radiation Sciences Program award numbers NNX07AL11G and NNX08AH57G. This research was supported by the NASA Earth Science Division Atmospheric Composition program award number NNH11AQ58UI. Author contributions: single-particle MS, EM, data analysis, and paper writing (D.J.C.); counterflow virtual impactor development, mass spectrometer development, single-particle MS, data analysis, and paper writing (K.D.F.); compilation of INAS densities from laboratory data, deriving the model-based estimates of upper tropospheric IN, and paper writing (C.H.); measurement of water vapor mixing ratio, analysis of relative humidity data, and paper writing (J.B.S., M.A.Z, and M.D.); mission planning, data analysis, and paper writing (E.J.J); TC4 instrument design and data acquisition, paper writing (C.H.T.); and mass spectrometer development, single-particle MS, data analysis, and paper writing (D.M.M.).

Supplementary Materials

www.sciencemag.org/cgi/content/full/science.1234145/DC1
Materials and Methods
Figs. S1 to S4
Tables S1 to S4
References (*33*–*71*)

17 December 2012; accepted 18 April 2013
Published online 9 May 2013;
10.1126/science.1234145

Epistasis Among Adaptive Mutations in Deer Mouse Hemoglobin

Chandrasekhar Natarajan,[1] Noriko Inoguchi,[1] Roy E. Weber,[2] Angela Fago,[2] Hideaki Moriyama,[1] Jay F. Storz[1]*

Epistatic interactions between mutant sites in the same protein can exert a strong influence on pathways of molecular evolution. We performed protein engineering experiments that revealed pervasive epistasis among segregating amino acid variants that contribute to adaptive functional variation in deer mouse hemoglobin (Hb). Amino acid mutations increased or decreased Hb-O_2 affinity depending on the allelic state of other sites. Structural analysis revealed that epistasis for Hb-O_2 affinity and allosteric regulatory control is attributable to indirect interactions between structurally remote sites. The prevalence of sign epistasis for fitness-related biochemical phenotypes has important implications for the evolutionary dynamics of protein polymorphism in natural populations.

Nonadditive interactions between mutations (epistasis) can exert a strong influence on the rate and direction of evolutionary change (*1*, *2*). Insights into mechanisms of epistasis between beneficial mutations can reveal the causes of constraints on adaptive protein evolution (*3*–*10*). Mechanisms of epistasis are often best revealed through detailed examinations of interactions between amino acid mutations in the same protein that contribute to variation in a measurable biochemical phenotype (*7*, *9*–*15*). Such studies are especially relevant to our understanding of evolutionary process when genetically based changes in the measured phenotype contribute to variation in fitness under natural conditions.

We investigated the nature of epistatic interactions between adaptive mutations in the hemoglobin (Hb) of deer mice (*Peromyscus maniculatus*). Deer mice that are native to high altitude have evolved an elevated Hb-O_2 affinity relative to lowland conspecifics (*16*–*18*), and this modification of protein function contributes to an adaptive enhancement of whole-animal physiological performance under hypoxia (*19*, *20*). Comparisons between highland deer mice from the Rocky Mountains and lowland deer mice from the Great Plains revealed genetic differences in Hb-O_2 affinity that are attributable to the independent or joint effects of 12 amino acid polymorphisms: 8 mutations in the α-chain subunits of the $\alpha_2\beta_2$ Hb tetramer, and 4 mutations in the β-chain subunits. These 12 amino acid polymorphisms exhibit pronounced altitudinal shifts in allele frequency, and population genetic analyses of nucleotide variation in the α- and β-globin genes revealed evidence for divergent selection between deer mouse populations that are native to different elevations (*18*, *21*–*23*).

Structural variation in deer mouse Hb has a modular organization that reflects the linkage arrangement of the 12 amino acid polymorphisms. Within the α-chain subunit, five amino acid replacements are located in exon 2 of the underlying gene, and the remaining three replacements are located in exon 3. Polymorphic sites within the same exon are in nearly complete linkage disequilibrium (LD) with one another, but intragenic recombination has produced a partial uncoupling between the two exons (*21*, *23*). The two most common α-globin allele classes are distinguished from each other by eight amino acid replacements at sites 50, 57, 60, 64, 71, 113, 115, and 116 (fig. S1A). The four amino acid polymorphisms in the β-globin gene are also in nearly complete LD with one another (*18*, *22*). The two most common β-globin allele classes are distinguished from each other by four amino acid replacements at sites 62, 72, 128, and 135 (fig. S1B). Thus, in deer mouse populations, most of the naturally occurring variation in Hb

[1]School of Biological Sciences, University of Nebraska, Lincoln, NE 68588, USA. [2]Zoophysiology, Department of Bioscience, Aarhus University, DK-8000 Aarhus, Denmark.

*Corresponding author. E-mail: jstorz2@unl.edu

Clarifying the Dominant Sources and Mechanisms of Cirrus Cloud Formation

Daniel J. Cziczo *et al.*

Science **340**, 1320 (2013);
DOI: 10.1126/science.1234145

Science (print ISSN 0036-8075; online ISSN 1095-9203) is published weekly, except the last week in December, by the American Association for the Advancement of Science, 1200 New York Avenue NW, Washington, DC 20005.